Chapter 4

Synthesis and Characterization Methods

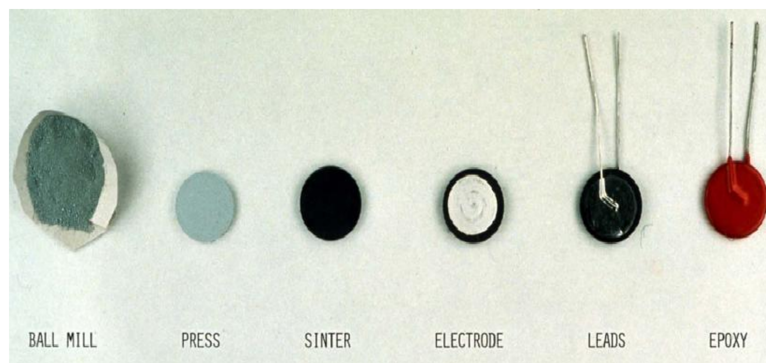

CHAPTER 4

Synthesis and Characterization Methods

In this chapter, the synthesis of the compounds selected for the present work and the experimental techniques employed to characterize the specimens, are briefly discussed.

Ceramic materials are one of the essential groups in the materials science because of their wide applications in day to day life. Hence the synthesis of new ceramic powders is of great importance in the progress of materials science. There are several methods of preparation such as mechanical method, which includes ball milling and solid-state reaction, etc., and the chemical method, which includes sol-gel, wet-dry and polymer-sol-gel etc. To achieve a quality product with respect to purity, homogeneity, reactivity, particle size etc. each method have its own advantages and disadvantages. In this context, the solid-state reaction found to be the easier, convenient and low cost technique among other available methods by means of performance, reliability, reproducibility and economy.

4.1. Synthesis of Specimens

A schematic scheme of processing and characterization of ZnO Varistor samples is given in Figure 4.5 and described in the following section;

4.1.1. Materials Used

Reagent grade high purity Sigma-Aldrich: ZnO (>99.00%), V_2O_5 (99.60%), Nb_2O_5 (99.99%), $MnCO_3$ (99.90%) Cr_2O_3 (99.50%) and ZrO_2 (99.50%) were used as raw materials. To investigate the effect of doping and sintering temperature, different compositions were prepared using solid state reaction. The grade, molecular weight, purity (%) and manufacture of raw materials used are shown in Table 4.1.

Table 4.1 Material used:

S. No.	Raw material used	Grade	Molecular Weight	Purity (%)	Manufacture
1.	ZnO	A.R /ACS	81.41	>99.00	Sigma Aldrich
2.	V_2O_5	A.R	181.88	99.60	
3.	Nb_2O_5	A.R	197.35	99.50	
4.	$MnCO_3$	A.R	115.00	99.90	
5.	Cr_2O_3	A.R	151.99	99.50	
6.	ZrO_2	A.R	123.22	99.50	

4.1.2. Weighing and Milling

Individual constituents were proportioned for a batch of 15/25gms. Mixing in an agate mortar was done for four hours using acetone to homogenize the batch. Then all the compositions were mixed homogeneously by conventional ball milling as shown in Fig. 4.1 with zirconia balls and acetone in a poly-propylene bottle for 24 h at 50rpm.

Figure 4.1: Conventional ball mill

4.1.3. Compaction

Thereafter, the mixtures were filtered, dried at 120 °C for 12 h and calcined at 650 °C for 3 h. The agglomerate was pulverized using an agate mortar-pestle pestle for about 3 hours to achieve fine powder and then granulated by sieving 100-mesh screen to produce starting powder. The powder was uniaxially pressed into pellets of diameter 12.50 mm and width 1.25 mm in a hydraulic press (shown in Fig. 4.2) at 10 ton load/150MPa pressure using polyvinyl butyral (PVB) as a binder. Initially the pressure was optimized by making pellets at different pressures and determining their green bulk density.

Figure 4.2: A 25 Ton hydraulic press and an oven

4.1.4. Sintering

After quality check selected pellets were placed inside a muffle furnace as shown in Fig. 4.3. The pellets were covered with protecting powdered and placed inside closed double alumina crucible at a different sintering temperature 850, 900 and 950 °C for soaking period of 3 hours with heating and cooling rate of 3 °C/min. During the sintering stage, a certain amount of pure V_2O_5 powders was simultaneously placed inside closed double alumina crucible to restrain V_2O_5 volatilization loss from the specimens.

Figure 4.3: Muffle furnace with programmable controller.

4.1.5. Lapping and Electroding

Before electrical measurements, sintered specimens as shown in Fig. 4.4 were lapped and polished to 1.0 mm thickness with emery paper on both sides and then annealed at 700 °C for 3 h to stabilize the electrical properties. Conductive silver paste was coated on both faces of the pellets and the electrodes were formed by curing it at 600 °C for 10 min.

Figure 4.4: Photographs of sintered ZnO-V_2O_5 sample.

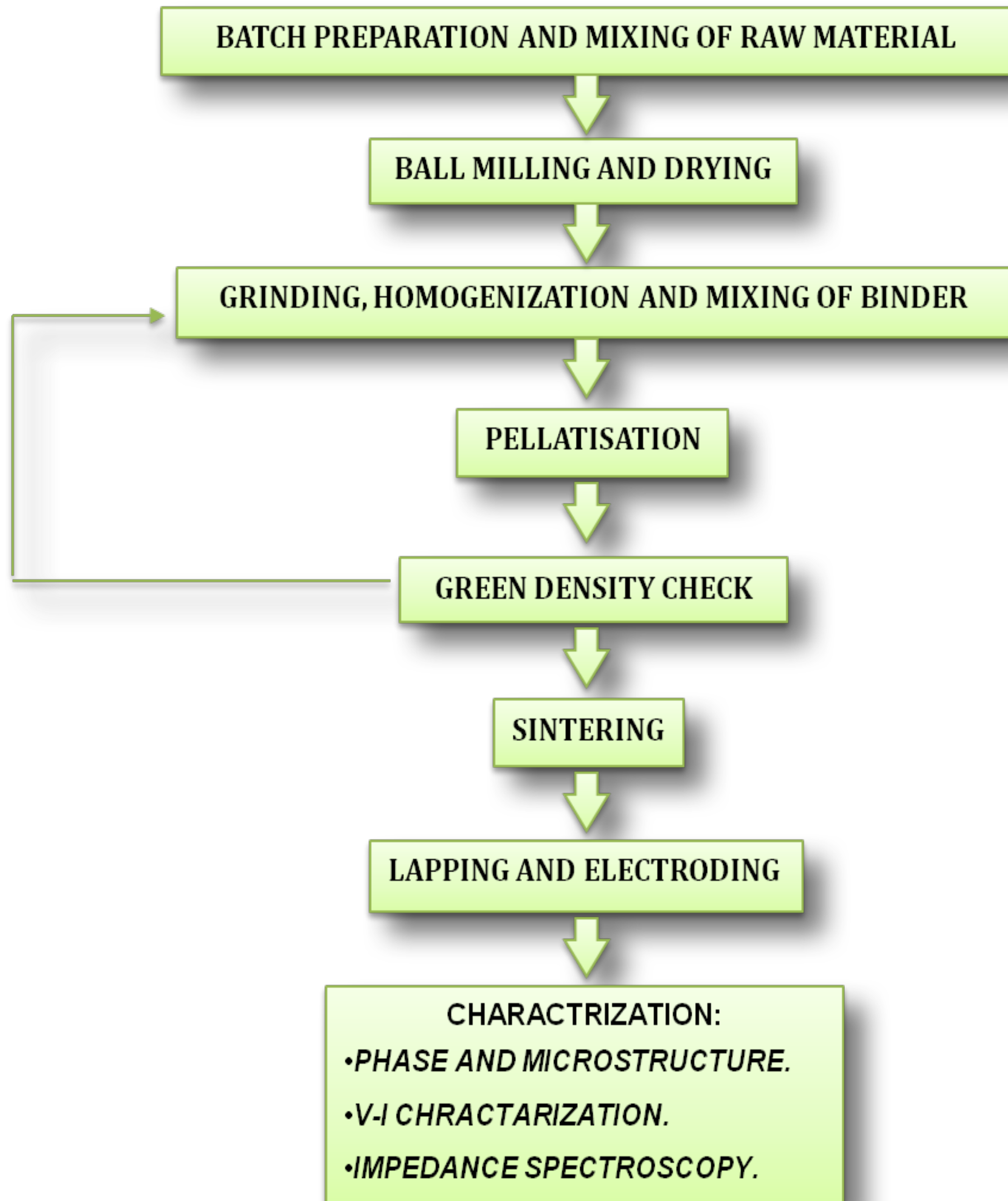

Figure 4.5: Processing and characterization of ZnO varistor

4.2. Characterization Techniques

4.2.1. X-Ray powder diffraction (XRD):

X-ray powder diffraction (XRD) is a rapid analytical technique primarily used for phase identification of a crystalline material and can provide information on unit cell dimensions. The analyzed material is finely ground, homogenized, and average bulk composition is determined.

Fundamental Principles of X-ray Powder Diffraction (XRD): Max von Laue, in 1912, discovered that crystalline substances act as three-dimensional diffraction gratings for X-ray wavelengths similar to the spacing of planes in a crystal lattice. X-ray diffraction is now a common technique for the study of crystal structures and atomic spacing.

X-ray diffraction is based on constructive interference of monochromatic X-rays and a crystalline sample. These X-rays are generated by a cathode ray tube, filtered to produce monochromatic radiation, collimated to concentrate, and directed toward the sample. The interaction of the incident rays with the sample produces constructive interference (and a diffracted ray) when conditions satisfy Bragg's Law ($n\lambda=2d \sin \theta$). This law relates the wavelength of electromagnetic radiation to the diffraction angle and the lattice spacing in a crystalline sample. These diffracted X-rays are then detected, processed and counted. By scanning the sample through a range of 2θ angles, all possible diffraction directions of the lattice should be attained due to the random orientation of the powdered material. Conversion of the diffraction peaks to d-spacings allows identification of the mineral because each mineral has a set of unique d-spacings. Typically, this is achieved by comparison of d-spacings with standard reference patterns. All diffraction methods are based on generation of X-rays in an X-ray tube. These X-rays are directed at the sample, and the diffracted rays are collected. A key component of all diffraction is the angle between the incident and diffracted rays. Powder and single crystal diffraction vary in instrumentation beyond this. Principle and arrangement of X-ray Powder Diffraction (XRD) are shown in Figure 4.6.

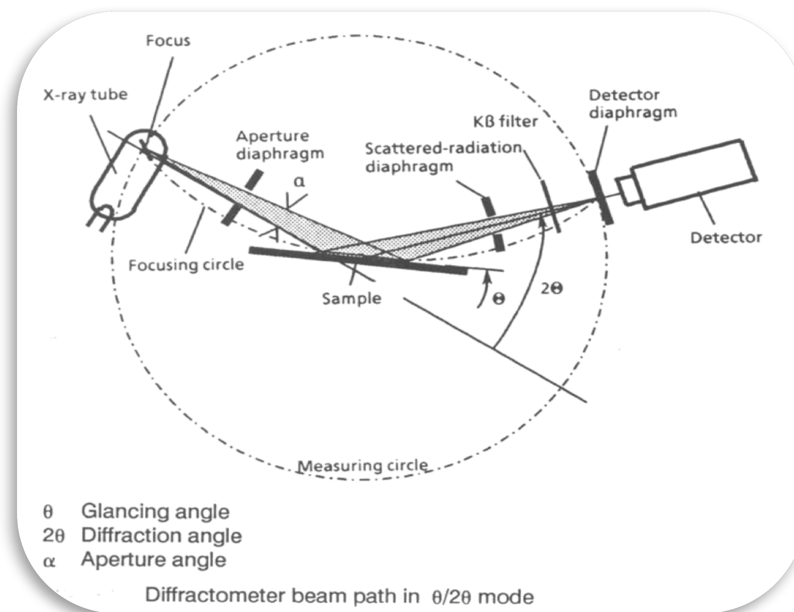

Figure 4.6: Principle and arrangement of X-ray Powder Diffraction (XRD)

X-ray Powder Diffraction (XRD) Instrumentation*:* X-ray diffractometers consist of three basic elements: an X-ray tube, a sample holder, and an X-ray detector as shown in Fig. 4.7. X-rays are generated in a cathode ray tube by heating a filament to produce electrons, accelerating the electrons toward a target by applying a voltage, and bombarding the target material with electrons. When electrons have sufficient energy to dislodge inner shell electrons of the target material, characteristic X-ray spectra are produced. These spectra consist of several components, the most common being K_{α} and K_{β}. K_{α} consists, in part, of $K_{\alpha1}$ and $K_{\alpha2}$. $K_{\alpha1}$ has a slightly shorter wavelength and twice the intensity as $K_{\alpha2}$. The specific wavelengths are characteristic of the target material (Cu, Fe, Mo, Cr). Filtering, by foils or crystal mono-chrometers, is required to produce monochromatic X-rays needed for diffraction. $K_{\alpha1}$ and $K_{\alpha2}$ are sufficiently close in wavelength such that a weighted average of the two is used. Copper is the most common target material for single-crystal diffraction, with Cu-K_{α} radiation = 1.5418Å. These X-rays are collimated and directed onto the sample. As the sample and detector are rotated, the intensity of the reflected X-rays is recorded. When the geometry of the incident X-rays impinging the sample satisfies the Bragg Equation, constructive interference occurs and a peak in intensity occurs.

A detector records and processes this X-ray signal and converts the signal to a count rate which is then output to a device such as a printer or computer monitor.

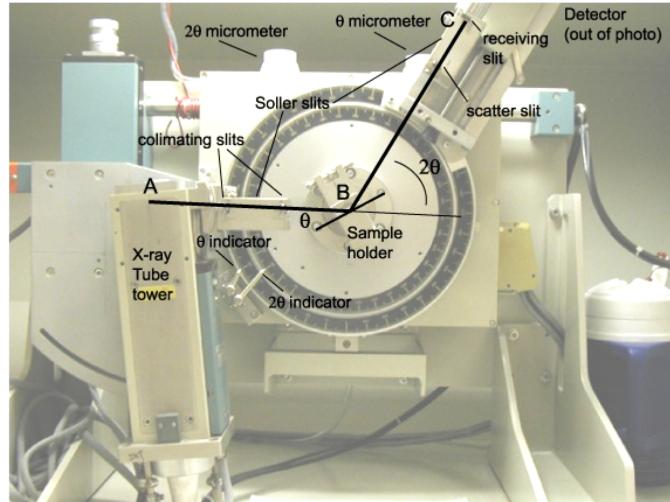

Figure 4.7: Figure of X-Ray Diffractometer

Powder X-ray diffraction patterns were recorded using a Rigaku high resolution powder X-ray diffractometer employing Cu-$K_{\alpha 1}$ radiation and Ni-filter. Data were collected in the 2θ range from 20 to 80°.

The average crystallite size, D, of the prepared powder has been calculated from the Scherrer's formula:

$$D = \frac{0.94\lambda}{\beta COS\theta} \tag{4.1}$$

where λ is the wavelength of the X-rays, θ is the diffraction angle and β is corrected full width at half maxima of the diffraction peak. The lattice parameters for hexagonal structure were calculated using 'Cell' software [Holland (1997)].

4.2.2. Scanning Electron Microscope (SEM):

Electron microscopes were developed in the 1930s to overcome the limitations of optical microscopy and provide increased magnification and resolution, far superior to optical systems. The first commercialized SEM was built by Cambridge Instruments [Goldstein J. I. (1992)].

SEM as shown in Fig. 4.8 is a powerful tool for examining and interpreting microstructures of materials, and is widely used in the field of material science. The principle of SEM is based on the interaction of an incident electron beam and the solid specimen [Grundy P. J. (1976)].

Electron bombardment can produce a wide variety of emissions from the specimen, including backscattered electrons, secondary electrons, Auger electrons, X-rays, visible photons and so on shown in Fig. 4.8.

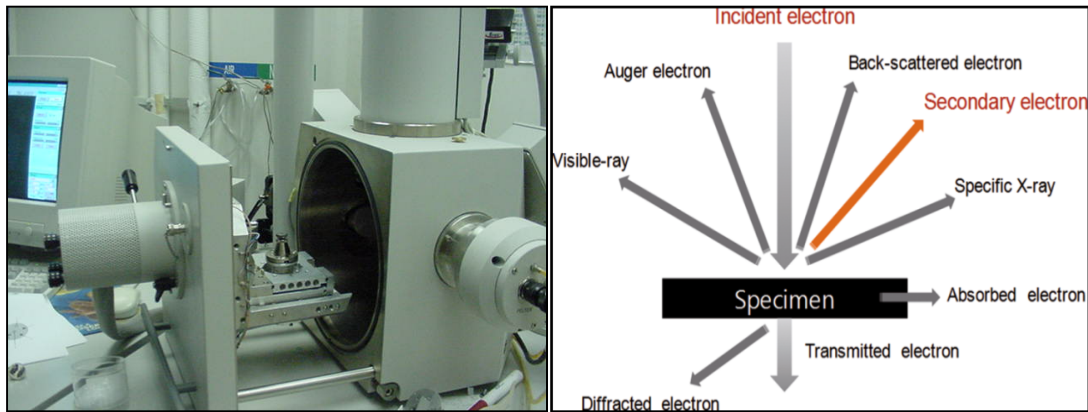

Figure 4.8: SEM device and the interaction of an incident electron beam

(a) Secondary Electrons: If an incident electron collides with an electron in a sample atom, it will knock the electron out of its orbital shell and the atom will become ionised. Because the incident electron loses little energy during each collision, multiple collisions are possible, continuing until the incident electron no longer has the energy to dislodge secondary electrons. Each freed secondary electron has a very small kinetic energy (<50 eV), which is independent of the incident electron energy. If generated close enough to the sample surface (<10 nm), these secondary electrons can escape to be collected by the detector. As a direct result, secondary electron imaging is closely related to sample topography.

(b) Backscattered Electrons: If an incident electron collides with the nucleus of surface atom, the electron will bounce or scatter 'backward'out of the sample as a backscattered electron (BSE). These electrons have high energies, typically between 50 eV and that of the original incident electron. The production of

backscattered electrons varies directly with atomic number, and thus backscattered electron images can be used to discern differences in sample atomic number.

(c) Auger Electrons**:** As a result of secondary electron generation, a vacancy is left in an ionized atoms electron shell. To fill this vacancy, an electron from a higher energy outer shell (from the same atom) can drop down to fill the vacancy. This creates an energy surplus in the atom that can be corrected by emitting an outer electron, an Auger electron. Auger electrons have a characteristic energy unique to the element from which they are emitted and can be used to give compositional information about the target sample. Auger electrons have a relatively low kinetic energy and are only emitted from shallow sample depths (<3 nm).

(d) **Characteristic X-rays:** X-rays are also produced by interactions of the incident electron beam with a sample surface. Similar to the Auger electron generating process, the excess energy produced by reshuffling electrons to fill shell vacancies can also be emitted in the form of an X-ray rather than an Auger electron. X-rays have a characteristic energy unique to the element from which they originate and so provide compositional information about a sample.

Secondary electron imaging and X-ray analysis were the primary functions used for SEM sample characterisation in this study.

An SEM consists of three distinct parts: an electron column; a detection system; and a viewing system. Figure 4.9 shows a schematic of a simple scanning electron microscope. Two electron beams are controlled simultaneously by the same scan generator: one is the incident electron beam; the other is for the cathode ray tube (CRT) screen. The incident beam is scanned across the sample, line by line, and the signal from the resulting secondary electrons is collected, detected, amplified and used to control the intensity of the second electron beam. Thus a map of intensity of secondary electron emission from the scanned area of the sample will be shown on the CRT screen as variations in brightness, reflecting the surface morphologies of the specimen. Given this mechanism, the

magnification of the SEM image can be adjusted simply by changing the dimensions of the area scanned on the sample surface.

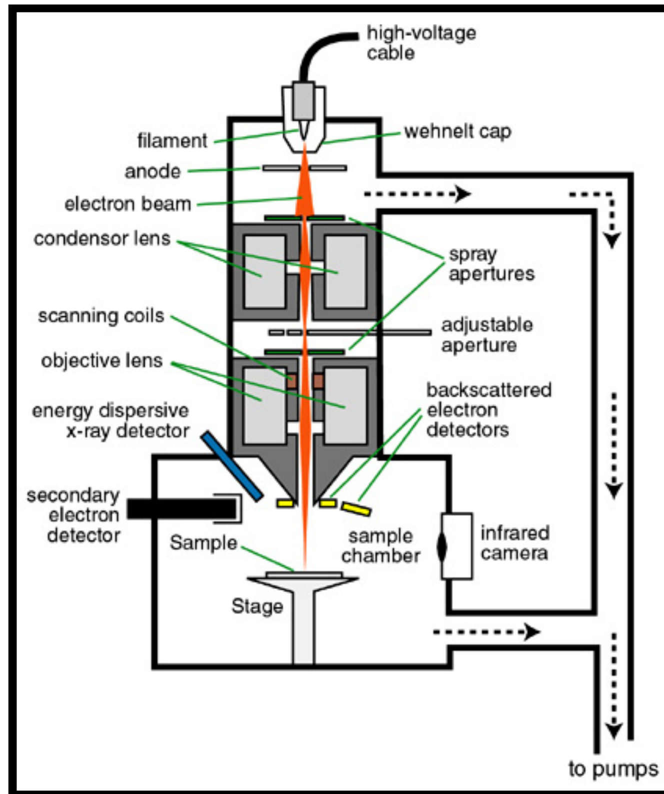

Figure 4.9: Shows a schematic of a simple scanning electron microscope.

The spatial resolution of the SEM is strongly dependent on diameter (spot size) of the electron probe beam at the specimen surface. In a SEM system, the diameter of the incident electron beam is de-magnified using two or more electron lenses before it reaches the sample surface. At the same time, the effective diameter of the electron source is a key factor in determining the resolution of the SEM. There are two basic types of electron guns in current use: thermionic electron gun and field emission electron gun. The diameters of the electron beam originating from these gun types are about 20-50 μm and 10 nm, respectively

For micro structural observations, the surfaces of the sintered pellets were lapped and ground with emery papers of grade 1/0, 2/0, 3/0, and 4/0 (Sia, Switzerland) followed by polishing on a velvet cloth with diamond paste of

grade1/4-OS-475 (HIFIN) to mirror-like finish. The polished surfaces were thermally etched to reveal the surface. ***The microstructure was examined by scanning electron microscopy (INSPECT 50 FEI).*** The average grain sizes G were measured directly from the micrographs of the etched samples by the lineal intercept method, as described by Mendelson (1972).

$$G = 1.56 \frac{L}{MN} \quad (4.2)$$

where L is the random line length on the micrograph, M is the magnification of the micrograph, and N is the number of the grain boundaries intercepted by lines.

EDS spectra and EDS elemental maps of the samples were recorded using a Zeiss EVO18 Research SEM attached with Oxford Instrument X-act.

4.2.3. Density

Density of the sintered pellets was determined by Archimedes principle using water as a medium. Theoretical density was determined from the molecular weight of the compound and lattice parameters using the relation:

$$\text{Theoretical density} = \frac{n \times \text{ gm.mol.wt.of sample}}{N \times (\text{unit cell})^3} \quad (4.3)$$

where n is no. of molecules of the compound in the unit cell, N is Avogadro's number, Sintered/Experimental density was calculated using the relation:

$$\text{Sintered/Experimental density} = \frac{W_a}{W_a - W_w} \quad (4.4)$$

where W_a and W_w, are weight of sintered pellet in air and water respectively.

Percentage theoretical density was calculated using the relation:

$$\text{Percentage theoretical density} = \frac{\text{Theoretical density}}{\text{Sintered/Experimental density}} \times 100 \quad (4.5)$$

4.2.4. Complex Plane Impedance Analysis

a) Sample Preparation:

Before electrical measurements, sintered specimens were lapped and polished to 1.0 mm thickness with emery paper on both sides and then annealed at 700ºC for 5 h to stabilize the electrical properties. Selected samples from quality control check were provided an ohmic contact on both the surfaces by coating with conductive Silver Paint and the electrodes were formed by curing it at 600°C for 10 min. Electrical characteristic of the sample were determine by Admittance analysis and I-V characteristics.

b) Immittance Analysis

Overall dielectric and electrical properties of polycrystalline electronic ceramics have contributions from (i) bulk or grains (ii) grain boundaries and (iii) electrode specimen interface or electrode polarisation. In order to understand the electrical behavior and to tailor make the useful properties, it is necessary to separate these contributions. Immittance analysis has emerged as a powerful and simple tool to separate the various contributions present in the electrical/ dielectric properties of electronic ceramics. It is useful in the studying defects, microstructure, surface chemistry and electrical conductivity of materials including dielectrics, ionic conductors and adsorbate-adsorbent interface. AC response of the materials can be expressed in any of the four basics formalism. These are complex impedance (Z^*), admittance (Y^*), electric modulus (M^*) and permittivity (ε^*) jointly referred to as immittance functions. These are related to one another as follows:

Impedance(Z^*)
$$Z^* = Z^{/} - iZ^{//} = \frac{1}{i\omega C_0 \varepsilon^*} \quad (4.6)$$

Admittance (Y^*)
$$Y^{//} = Y^{/} + iY^{//} = i\omega C_0 \varepsilon^* \quad (4.7)$$

Electric Modulus (M^*)
$$M^* = M^{/} + iM^{//} = \frac{1}{\varepsilon^*} \quad (4.8)$$

Permittivity (E^*)
$$\varepsilon^* = \varepsilon^{/} - i\varepsilon^{//} \quad (4.9)$$

$$\tan\delta = \frac{\varepsilon^{//}}{\varepsilon^{/}} = \frac{M^{//}}{M^{/}} = \frac{Y^{/}}{Y^{//}} = \frac{Z^{/}}{Z^{//}} \quad (4.11)$$

Where, ω is the angular frequency, ω = 2πf of applied electric field, f being the frequency in cycles/sec, C_0 is the geometrical capacitance.

The study of ε^* as a function of frequency has been widely used, It is most suited for dielectric materials having very low or vanishing conductivity. For electronic ceramics Z^*, Y^* and M^* are mostly used, which are used in the present investigations. Two types of plots may be generated (1) Complex plane plots e.g. $Z^{//}$ Vs $Z^{/}$ and $M^{//}$ Vs $M^{/}$ plots and (2) Spectroscopic plots $Z^{//}$ or $M^{//}$ vs. log f plots. For complex plane immittance analysis $Z^{//}$ and $Z^{/}$ or $M^{//}$ and $M^{/}$ are measured over a range of frequencies and plotted as $Z^{//}$ Vs $Z^{/}$ or $M^{//}$ vs. $M^{/}$. If a polycrystalline ceramic has contributions from grains, grain boundaries and electrode, then each of these contributions can be represented by a circuit element containing R and C connected in parallel. The sample can therefore be represented by an equivalent circuit containing three parallel RC circuit elements connected in series as shown in Fig 4.10.

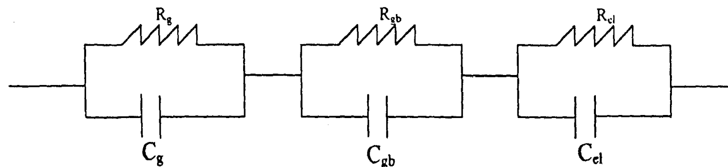

Figure 4.10: Equivalent circuit for a sample having grain, grain boundary and electrode polarisation processes

Here R_g, R_{gb} and R_{el} represent the resistive contributions of grains, grain boundaries and electrode polarisation process while C_g, C_{gb} and C_{el} represent their corresponding capacitive contributions respectively. In complex plane impedance and modulus analysis, one observes three semicircular arcs with their centers on the real axis if each of the above three contribution has a single value of relaxation time as shown in Fig. 4.11.

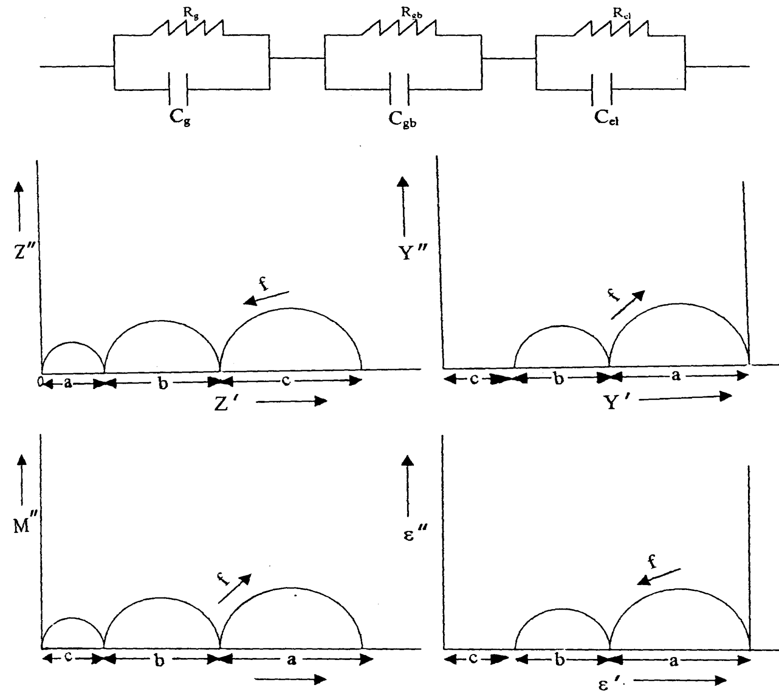

Figure 4.11: Equivalent circuit for a polycrystalline ceramic sample and corresponding frequency response in the complex plane plots for four electrical formalisms

Relaxation time τ which is equal to the inverse of the angular frequency, 'ω' at which the relaxation occurs, is given by the RC product i.e.

$$\tau = 1/\omega = RC \quad (4.11)$$

The equations for the real axis intercepts for various Immittance functions in complex plane plots. The intercepts of the arcs with the real axis ($Z^{/}$) give the resistive contributions R_g, R_{gb} and R_{el} in the impedance plots. The intercepts with $M^{/}$ axis in modulus plots are inversely proportional to the capacitive contributions (C_0/C_g, C_0/C_{gb} and C_0/C_{el}). The value of the capacitance from the impedance plots and resistance from the modulus plots can be obtained from the frequency of the highest point in the arc where the relation $\omega RC = 1$ is satisfied. Frequency increases in opposite direction in complex plane impedance and modulus plots.

The electrode polarisation process being most sluggish appear in the lowest frequency range followed by grain boundaries in the intermediate frequency range and bulk or grains contribution appear in the highest frequency range in the impendence and modulus plots. If any of the above contributions has a distribution of relaxation times rather than a single value, then one observes a depressed circular arc with its center below the $Z^{/}$ or $M^{/}$ axis. The angle, α, which the line joining the origin to the center of circle makes with real axis is a measure of distribution of relaxation times of that contribution. The actual number of arcs appearing in the complex plane plots also depends on the ratio of various times constant. An electronic ceramic having negligible value of electrode – specimen interface contribution, (ohmic contact) can be represented by two parallel RC elements connected in series. For such an equivalent circuit, complex plane impedance, modulus and admittance plots are simulated for different ratios of the two time constants. By comparing the experimental complex plane plots with these simulated plots one can propose a suitable equivalent circuit for a given sample.

Whether a full, partial or no semi circle is observed depends on the strength of relaxation, value of distribution parameters and the experimentally available frequencies. Strength of relaxation is defined as $\varepsilon_S / \varepsilon_\infty$ where ε_S is the value of static dielectric constant as $\omega \rightarrow 0$ and ε_∞ is the dielectric constant as $\omega \rightarrow \infty$ i.e. at optical frequencies. Therefore, it is not surprising that certain function is favored on other depending on whether the material being studied is insulating, semiconducting or conducting. It is clear from above discussion that impedance plots highlight circuit element (contribution) with large resistance (grain boundaries and electrode – specimen interface) while the modulus plots highlight the contribution with minimum capacitance (bulk contribution).

In the spectroscopic plots ($Z^{//}$ or $M^{//}$ vs. log f) one gets Debye – like peaks. The number of peaks observed depends on the ratio of time constant of the various contributions. The height of the peak in $Z^{//}$ vs. log f plot is given by R/2 where R is the resistive contribution of the process while the height in

modulus spectroscopic plots gives $C_0/2C$ where C_0 is the geometrical capacitance and C is the capacitive contribution. Therefore, normally contribution of grains being least resistive get suppressed in impedance spectroscopic plots while capacitive contribution of thin regions like grain boundaries and electrode – specimen interface gets suppressed in modulus spectroscopic plots. Therefore it is advantageous to analyze the immittance data in impedance and modulus form simultaneously because one can get complimentary information from the two types of plots. Capacitance of grains, being thick is in Pico-farad range (except for ferroelectric materials), that of grain boundaries are in nano farad range while electrode – specimen interface having minimum thickness have capacitance in microfarad range.

Spectroscopic plots are convenient to determine the relaxation frequencies while complex plane plots give resistive or capacitive contribution of various electrical processes or regions in the material. For an ideal Debye process with single value of relaxation time, the full width at half maximum (FWHM) is 1.14 decades. If FWHM is more than 1.14 decades, this indicates either a distribution of relaxation times or a summation of two or more overlapping relaxation processes. It is necessary to discuss the meaning of a relaxation time because it is often assumed in the literature that a particular physical property has a single relaxation time irrespective of what function is chosen to display it. This is not the case as each dielectric function has its own relaxation time. It, therefore, determines at what frequency the imaginary part of a particular dielectric function will have a peak ($\omega\tau = 1$). For a single relaxation process, It is found that $\varepsilon^{//}$, $Y^{//}$, $Z^{//}$ and $M^{//}$ peak at increasing frequency i.e. $\tau_{\varepsilon}^{//} > \tau_{Y}^{//} > \tau_{Z}^{//} \geq \tau_{M}^{//}$. The separation between various peaks depends on the strength of relaxation i.e. $\varepsilon_S/\varepsilon_\infty$ defined earlier. The separation increases with increasing value of relaxation ratio. The position of peaks help in determining whether a particular relaxation processes is localized (dipolar relaxation) or non – localized i.e. long range conductivity process. It has been shown that for a long range process, peaks in $Z^{//}$ and $M^{//}$ vs. log f plots will occur

at the same frequency even for a very large relaxation ratio while they will appear separately even for a small relaxation ratio.

The impedance spectroscopy was measured with an ***Alpha A High Performance Frequency Analyzer Novocontrol Technologies, Germany*** (Fig. 4.12) in the frequency range 10 mHz to 1 MHz with 1 V applied ac signal and temperature 323 K to 673 K. The sample was placed in a sample holder, kept in a container to shield it from any stray field. The sample holder was kept in a furnace and Immittance data for different samples were recorded in frequency range 10 mHz to 1MHz and in the temperature range from room temperature to 673 K.

Figure 4.12: An Alpha A High Performance Frequency Analyzer Novocontrol Technologies.

The obtained experimental results were fitted using commercially available **'Electrochemical Impedance Spectroscopy' (EIS) software** [Bondarenko et al. (2005)] for modeling and analysis of impedance spectroscopy measurements in terms of equivalent circuits involving resistors, capacitors, and/or a constant-phase element (CPE).

Impedance spectra were fitted to the equivalent circuits containing two parallel resistance-constant phase element sub circuits in series. Use of a simple capacitor is not sufficient to model the electrical response of the materials due to microstructural heterogeneities of the sample. The appearance of full, partial

semicircles or no semicircle depends upon the strength of relaxation and the available frequency range [Bueno et al. (1998)], though these semicircles are depressed. This behavior confirms the presence of a non-Debye type relaxation in the materials and also manifest that there is a distribution of relaxation times instead of a single relaxation time in the material. In most real cases relating to ceramic materials, the Nyquist plot is depressed with its center below the real axis. A perfect semicircle with center on the Z'-axis is observed for ideal Debye-type relaxation. However, in the studied material, we did not find such Debye-type relaxation [Tsai et al. (1994), (1996)]. To represent the non-ideal Debye type behavior, a constant phase element (CPE), which has impedance given by Abram et al. (2003), is introduced with the resistors and capacitors or CPE. CPE is equivalent to a distribution of capacitors in parallel. The impedance function of the CPE element is

$$Z_{CPE} = \frac{1}{P(j\omega)^n} \tag{4.12}$$

where ω =2πf is the angular frequency (f is the applied frequency in Hz), $j = \sqrt{-1}$; P is a constant that is independent of frequency, and n is an exponential index which is the measure of arc depression [West et al. (1997)]. The constant n equals 1 for ideal Debye-like behavior, in which case the CPE represents an ideal capacitor (C = P). The capacitor is frequency dependent when the n value is below unity, while for n = 0, the CPE acts as a pure resistor with value $R = 1/P$. In most real cases involving ceramic materials the arc in complex impedance plots of Im(Z') versus Re(Z") is depressed, with its center below the real axis. However, in polycrystalline semiconductors the trapping of the charge at grain boundaries seems to have a decisive influence on the electrical transport properties due to the formation of electrostatic potential barriers [Jorcin et al. (2006); Jonscher (1977)].

4.2.5. Dielectric Characteristics

The dielectric characteristics, such as the apparent dielectric constant (ε') and dissipation factor (tan δ) was measured with ***an Alpha A High Performance Frequency Analyzer Novocontrol Technologies, Germany*** in the frequency range 10 mHz to 1 MHz with 1 V applied ac signal and at 323 K to 523 K

4.2.6. Electric Field–Current Density (E–J) Characteristics

For the measurement of electric field–current density (E–J) characteristics the samples was placed in a sample holder (spring loaded) kept in a container to shield from any stray fields. The current through the sample and voltage across it was measured by an ***I–V source/measure unit Keithley 2410, U.S*** as shown in Fig. 4.13.

Figure 4.13: I–V source/measure unit Keithley 2410, U.S

The breakdown field (E_{1mA}) was measured at 1.0 mA/cm^2 and the leakage current density (J_L) was measured at 0.75 E_{1mA}. In addition, the nonlinear coefficient (α) is defined by the empirical law,

$$J = KE^{\alpha}, \tag{4.13}$$

where J is the current density, E is the applied electric field, and K is a constant. Nonlinear coefficient 'α' was determined in the current density range 1.0–10 mA/cm^2, where $\alpha = 1/(\log E_2 - \log E_1)$, and E_1 and E_2 are the electric fields corresponding to 1.0 and 10 mA/cm^2, respectively [Levinson et al. (1975); Hanada (2009)].